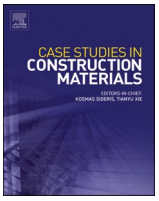
Case Studies in Construction Materials 22 (2025) e04802



Contents lists available at ScienceDirect

Case Studies in Construction Materials

journal homepage: www.elsevier.com/locate/cscm



Effects of 3D-printed concrete permanent formwork on the flexural behavior of reinforced concrete beams: Experimental and analytical investigations

Tae-Kyung Kim, Sangwoo Oh, Jinsuk Lee, Won-Jun Dong, Bunleang Mak, Seongcheol Choi, Chang-Su Shim *

Department of Civil and Environmental Engineering, Urban Design and Studies, Chung-Ang University, 84 Heukseok-ro, Dongjak-gu, Seoul 06974, Republic of Korea

ARTICLE INFO

Keywords:
3D concrete printing
Permanent formwork
Flexural strength
Anisotropic behavior
Equivalent strength
Strain compatibility method

ABSTRACT

In response to challenges such as skilled labor shortages, reduced productivity, and the slow pace of digital transformation, 3D concrete printing (3DCP) offers a promising solution. Despite the growing interest in 3DCP as a construction solution, existing studies have primarily focused on material-level behavior, while experimental verification of structural performance remains limited—particularly regarding the applicability of existing design codes and quality control specifications to members incorporating 3D-printed elements, highlighting the need for further structural-level investigations. To address this gap, this study examines effects of 3D-printed concrete permanent formwork (3DPF) on the flexural behavior of reinforced concrete (RC) beams. Two 3DPF and two cast-in-place beams were fabricated. Four-point bending tests evaluated crack patterns, failure modes, load–displacement relationships, and strain distributions, finding that 3DPF improved the flexural strength of RC beams, emphasizing its importance in structural design considerations. However, vertical crack patterns induced by weak interlayer bonding strength were observed, along with reduced displacement ductility in the 3DPF beams. Equivalent strengths between cast and printed materials were established to facilitate flexural strength analysis with cast specimens. A strain compatibility approach was proposed based on Eurocode 2, incorporating the equivalent strength of the printed material, an effective layer width, and the cross-sectional geometry of the 3DPF beam. The calculated values using this approach showed good agreement with the experimental results for nominal flexural strength and neutral axis depth.

1. Introduction

The construction industry encounters numerous challenges compared to other manufacturing sectors, including a decline in skilled labor, reduced productivity, and a slow rate of digital transformation [1–3]. 3D concrete printing (3DCP) has emerged as a promising solution to address these issues. This technology offers distinct advantages, such as reducing labor requirements and enabling the precise fabrication of complex shapes, surpassing conventional methods that rely on temporary formwork systems [4–9]. However,

* Corresponding author.
E-mail address: csshim@cau.ac.kr (C.-S. Shim).

https://doi.org/10.1016/j.cscm.2025.e04802

Available online 28 May 2025
2214-5095/© 2025 The Author(s). Published by Elsevier Ltd. This is an open access article under the CC BY-NC-ND license (http://creativecommons.org/licenses/by-nc-nd/4.0/).

while significant advancements have been made in materials and printing systems, the structural behavior of members fabricated through 3DCP remains insufficiently characterized. To elevate 3DCP technology to practical applications, it is critical to resolve structural uncertainties and establish robust design methodologies [10,11].

Recent research into 3D-printed concrete flexural members has proposed innovative member shapes, assembly techniques, and reinforcement strategies compared to conventional reinforced concrete (RC) members [12–19]. These studies have introduced approaches for fabricating flexural members using 3DCP. Nevertheless, substantial barriers continue to obstruct the practical adoption of 3DCP in structural member fabrications. Key challenges encompass the anisotropic nature of 3DCP materials and brittle failures resulting from weak interlayer bonding strength [20–23]. The anisotropic behavior of these materials indicates that their performance may vary depending on the orientation of the printed layers, while low interlayer bonding strengths can critically affect failure mechanisms in both members and materials [24–27]. Although previous studies have reported these findings, the structural members evaluated so far have been limited in terms of geometry, materials, and fabrication methods. Therefore, there are still limitations in comprehensively verifying how the anisotropic behavior and weak interlayer bonding of printed materials interact with conventional concrete and steel reinforcements, which are essential components of structural members, and influence overall structural performance. Notably, discontinuities in material composition or geometry within the beam cross-section can affect flexural performance indicators, such as initial stiffness, ductility, and energy absorption capacity [28].

Furthermore, current design codes are primarily based on conventional RC members, not considering the applicability to 3D-printed concrete members [18,19]. To effectively utilize and develop current design codes to 3D-printed concrete members, verifying the specific differences that arise as compared to conventional methods is essential. First, it is crucial to assess whether the results of 28-d standard compression tests are applicable to 3DCP members for calculating ultimate flexural strength. Unlike conventional cast members, printed members feature interfaces, and the lack of a vibration process increases the likelihood of voids. Additionally, periodic strength evaluations during member fabrication are inefficient owing to the challenges in accurately cutting printed members to produce test specimens. Thus, a method to convert the strength of cast materials to that of printed materials is necessary. Second, it must be determined whether the composite behavior of the printed material and cast-in-place concrete in the compression zone under bending moments can be assumed to match that of conventional RC members. EN 1992–1–1: Eurocode 2 [29] assumes a concrete compressive strain of 0.0035, while ACI 318–05 [30] assumes 0.003. Addressing these challenges will enable the development of more accurate and reliable design codes for the structural analysis and design of 3DCP members.

The main objectives of this study were to evaluate the effects of 3D-printed concrete permanent formwork (3DPF) on the flexural behavior of beams and to examine the applicability of existing strain compatibility method through comparisons with conventional RC beams. This study presents an experimental investigation into the flexural behavior of 3DPF beams, compares the results with those of RC beams, and proposes a nominal flexural strength analysis process for 3DPF beams. Specifically, four-point bending tests were conducted on four beams: two 3DPF beams and two RC beams. The study analyzed crack patterns, failure modes, load–displacement relationships, and strain distributions of the beams. Then, the experimental results were compared with the results of the strain compatibility method based on Euroecode 2. This analytical method incorporates equivalent strength between the printed and cast materials, as well as the effective layer width, and section analysis. Ultimately, the contribution of this study lies in evaluating the anisotropic behaviors of RC beams fabricated through a novel method with 3DCP, which has remained unverified in previous literature. It also validates the applicability of an existing design code and proposes specific methods for achieving more accurate analysis.

2. Material

2.1. Raw materials and mix proportions

The fineness and density of type I ordinary Portland cement (OPC; CEM I) used were 3499 cm^2/g and 3.13 g/cm^3, respectively. Table 1 presents the chemical composition of the cement. Feldspar (medium particle size: 268 μm; density of 1.5 g/cm^3) were selected as fine aggregate to ensure pumpability, improve mechanical properties, and reduce material cost, given their local availability in South Korea [31]. The superplasticizer (SP) used was a polycarboxylate ether type (EcoCrete, ECONEX® Co., Ltd., Seoul, Korea) with a density of 1.06 g/cm^3 and a pH of 6.5. The viscosity-modifying admixture (VMA) used was a methyl hydroxyethyl cellulose type (Combizell® LH20M, Tianpu Chemicals Co., Ltd., Zhangjiagang, China), characterized by a density of 0.35 g/cm^3 and a viscosity of 20,000 mPa·s. It is commonly employed in cement-based materials to mitigate segregation by enhancing the viscosity of the fresh mixture

Table 1
Chemical composition of the cement used in the study.

Chemical composition	Chemical formula	Content [%]
Lime	CaO	61.80
Silica	SiO_2	21.23
Alumina	Al_2O_3	5.36
Ferrite	Fe_2O_3	3.20
Magnesia	MgO	2.38
Sulfur trioxide	SO_3	2.07
Potassium oxide	K_2O	0.69
Sodium oxide	Na_2O	0.08
Loss on ignition	LOI	2.94

[32]. Fig. 1 illustrates the particle size distributions of cement, VMA, and fine aggregates, determined using a laser diffraction particle size analyzer (Mastersizer 3000, Malvern Instruments Ltd.). The median particle sizes of cement, VMA, and fine aggregates were 16.5, 85.6, and 268 μm, respectively. Fine particles and well-graded particle size distributions improve flowability and early strength, which are essential for ensuring pumpability and buildability in 3D printable cement-based materials [33].

The 3D printing mortar (3DPM) used in this study had a water–cement ratio of 0.30 and a fine aggregate–cement ratio of 1.22. To achieve the desired printability, the SP dosage was set at 1.65 % by weight of the cement, while VMA was added at a dosage of 0.2 % by weight of the cement, a commonly used proportion for 3D printable mixes. During the mixing process, the dry materials, including cement, fine aggregate, and VMA, were mixed for 60 s. Approximately 80 % of the total water was gradually added to the dry materials within 30 s, and the SP was incrementally incorporated to ensure uniform distribution. Subsequently, the remaining water was added, and the mixture was blended for an additional 180 s. The mixing sequence and duration are critical for achieving material homogeneity, which is particularly important in 3D printing applications. Inadequate homogeneity can introduce uncertainties in extrusion quality, as the printing process involves applying high pressure to extrude the material through a nozzle [34]. The cast-in-place concrete (CIPC) was a ready-mixed concrete prepared with Type I ordinary Portland cement. It had a nominal strength of 35 MPa and a slump of 120 mm. The maximum particle size of the coarse aggregate was 25 mm. The water–cement ratio and fine aggregate ratio of the CIPC were 0.34 and 46.8 %, respectively. The 28-d mean compressive strength of the CIPC was 39.58 MPa, based on tests conducted on three standardized 100 mm × 200 mm cylindrical specimens following ASTM C39/C39M [35].

2.2. Lab-scale preliminary tests

To validate the performance of 3DPM from a 3D printing perspective, lab-scale preliminary tests were conducted. The fresh properties of 3DPM were quantified using a flow table test (ASTM C 1437 [36]), a penetration resistance test (ASTM C 403 [37]), and rheology tests. Rheology tests were performed using an ICAR Plus rheometer (ICAR Plus Rheometer, Germann Instruments, Inc.) [38]. Fig. 2 presents the methodologies for measuring the torque response of 3DPM, along with representative measurements corresponding to these protocols. Fig. 2**(a)** depicts the rotation of a vane at a constant low velocity (0.025 rps) for 60 s. Based on the data obtained, the static yield stress of 3DPM was calculated at intervals of 0, 1, 3, 5, 10, 20, and 30 min of resting time, and the structural build-up (A_{thix}) of 3DPM was determined. This evaluation is critical for assessing the material's capacity for layer deposition without plastic collapse (i.e., buildability). The derivation and calculation processes are detailed in [39,40]. Fig. 2**(b)** illustrates the methodology of sequentially reducing the vane rotation velocity from 0.5 rps to 0.05 rps over 60 s in 12 steps of 5 s each. Using the modified Bingham model proposed by Feys et al. [41], the dynamic yield stress and plastic viscosity were determined. A detailed explanation of the calculation process is available in [39]. Table 2 summarizes the fresh properties of 3DPM, as measured by the flow table test, the penetration test, and rheology tests. All the lab-scale preliminary tests were conducted indoors, where the average temperature and humidity were 15 ± 1℃ and 16 ± 1 %, respectively.

3D concrete printing experiments are inherently costly and time-intensive. Additionally, inappropriate material selection can result in pipe blockages, leading to potential breakdowns of the printer or pump [42]. To mitigate these inefficiencies, simple tests were conducted to evaluate pumpability, extrudability, and buildability. A self-made slug-test apparatus, shown in Fig. 3**,** was used to assess the pumpability and extrudability of 3DPM. The slug-test is a novel method for inline measurement of the yield stress of gravity-induced non-newtonian flow exiting the nozzle [43,44]. In this method, the mass of droplets, referred to as "slug," from the freely falling extruded material is measured. These measurements can be converted into yield stress under the assumption that the

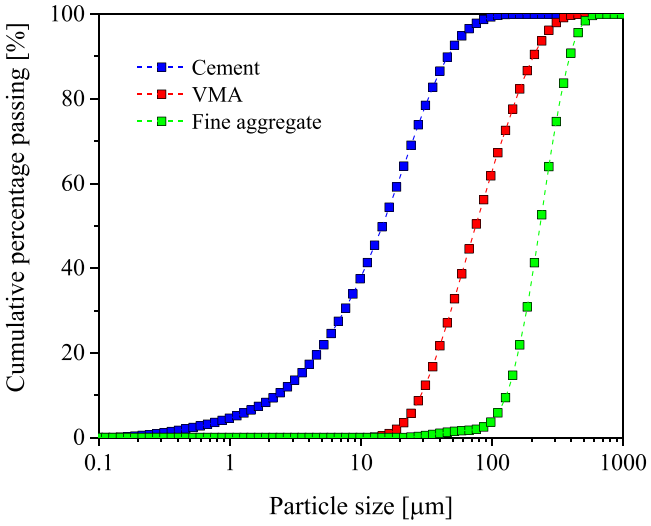


Fig. 1. Particle size distributions of cement, VMA, and fine aggregate.

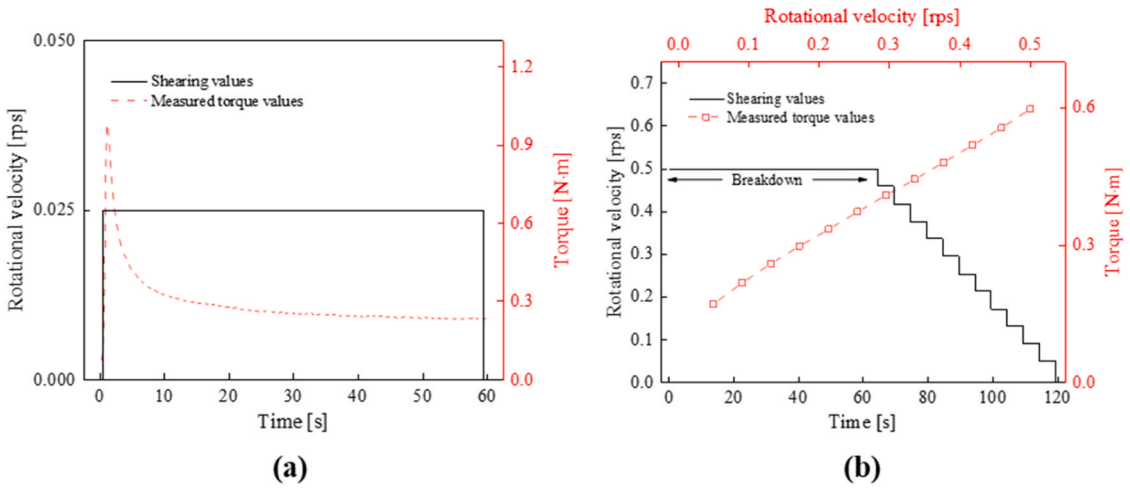


Fig. 2. Rheological measurement protocols (a) stress growth test used to determine static yield stress and structural build-up, and (b) flow curve test used to determine dynamic yield stress and plastic viscosity.

Table 2
Fresh properties of 3DPM.

Flow spread [mm]	Initial setting time [min]	Final setting time[min]	A_{thix} [Pa/s]	Dynamic yield stress [Pa]	Plastic viscosity[Pa·s]
149 ± 2	570	735	1.079	1848 ± 150	177 ± 22

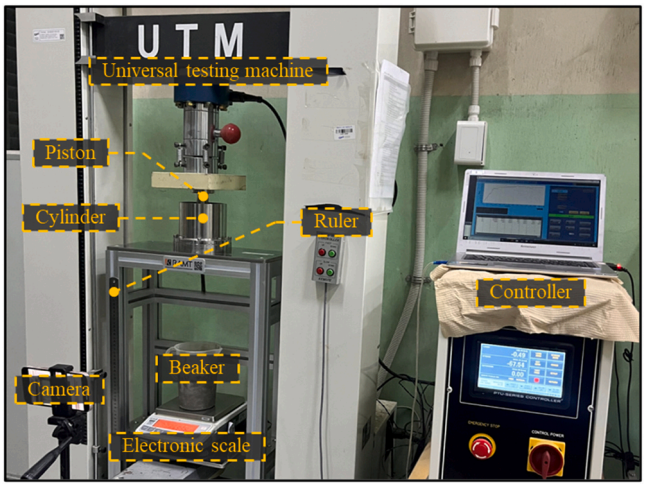


Fig. 3. Self-made slug-test setup for simple evaluation of pumpability and extrudability.

extruded material behaves as a purely plastic yield stress fluid without viscous contributions [45]. However, in this study, the high viscosity of the 3DPM made it impossible to neglect the viscosity's influence. Therefore, the evaluation of pumpability and extrudability was limited to measuring extrusion pressure and assessing layer continuity. For real applications with the 3D concrete printer used in this study, a nozzle diameter of 22.5 mm was used. The extrusion pressure of 3DPM was recorded as 18.22 kPa at 15 min, 23.35 kPa at 35 min, and 36.91 kPa at 65 min after the contact between cement and water. The corresponding drop masses of 3DPM at these times were 55.97 ± 2.71 g, 48.05 ± 3.24 g, and 40.32 ± 3.87 g, respectively. The extrusion pressure required after 1 h was 2.2 times higher than that at 15 min, while the continuity of the extruded material decreased by 27.97 % after more than 1 h compared to its state at 15 min. To address these challenges, the batch quantity for actual scale printing was carefully managed to ensure that the contact time between cement and water did not exceed 1 h. Buildability, which includes deposition capacity and layer deformation, was evaluated using a simple vertical deposition test. The 3DPM was deposited in 10 layers using a nozzle with a 22.5 mm diameter, as shown in Fig. 4**(a)**. After the final set, the 3D-printed material was cut using a concrete saw, and the average widths of the 2nd, 3rd, and

4th layers from the bottom were compared with those of the 7th, 8th, and 9th layers to assess layer deformation, as illustrated in Fig. 4 **(b)**. This assessment helped determine the appropriate time gap between layers for printing the actual scale 3DPF.

2.3. Equivalent compressive and flexural strengths of 3DPM

Printed and cast specimens were fabricated to establish equivalent strengths between the two types of specimens for both analytical purposes and simplified quality control of printed structures. Two types of specimens were tested for the compressive strength, as shown in Fig. 5: printed cube specimens with dimensions of 37.5 mm × 37.5 mm × 37.5 mm, corresponding to the actual thickness of the 3DPF, and cast cube specimens fabricated according to ASTM C109/C109M, with dimensions of 50 mm × 50 mm × 50 mm [46]. Similarly, two types of specimens were tested for flexural strength, as shown in Fig. 6: printed beam specimens with dimensions of 37.5 mm × 37.5 mm × 150 mm, reflecting the actual 3DPF thickness, and cast beam specimens measuring 40 mm × 40 mm × 160 mm which were prepared in accordance with ASTM C348 [47].

A total of ten printed specimens and three cast specimens were fabricated for each test type. The printed specimens were cut using a band saw after the initial setting time of the 3DPM. All specimens were wrapped and cured under I dentical conditions with the 3DPF for 28-d. During compression tests, the load was applied orthogonally to the layer direction. In flexural tests, the load was applied parallel to the layer direction to simulate the behavior of actual flexural members in this study as shown in Fig. 5. All strength evaluations of the 3DPM were conducted under the same environmental conditions as the lab-scale preliminary tests.

Table 3 lists the 28-d mean compressive strength results of each specimen type. The material strength tests were conducted using a universal testing machine. The printed cube specimen showed 59.40 % lower compressive strength compared to that of the cast cube specimen (Eq. (1)).

$$f_{cm,3D} = 0.59 f_{cm,cast} \tag{1}$$

Table 4 lists the 28-d mean flexural strength results for each specimen type. The flexural strength tests were conducted using a universal testing machine. The flexural strength of the printed beam specimens was 51.35 % of that of the cast beam specimens, and expressed as Eqs. (2), and 8% of that of the cast cube specimens, as expressed in Eq. (3).

$$f_{rm,3D} = 0.51 f_{rm,cast} \tag{2}$$

$$f_{rm,3D} = 0.08 f_{cm,cast} \tag{3}$$

Both the compressive and flexural strengths of the printed specimens showed noticeably higher CoV compared to those of the cast specimens. In this study, the result was associated with inconsistent nozzle extrusion in the layer-by-layer deposition method, which is less reliable and robust than conventional casting [48]. The manual extrusion process used in this study, which involved a nozzle not connected to a fully automated pumping system and required continuous material feeding by hand, led to variations in extrusion rate and time intervals between layers. These process-induced inconsistencies, combined with the high structuration rate of the printing material, were considered potential factors that increased the CoV observed in the printed specimens [49]. Considering that RC structures are designed based on the nominal strength of materials, the higher variance in the strength data of printed materials suggests that a lower strength reduction factor will be required than that typically used for conventional concrete.

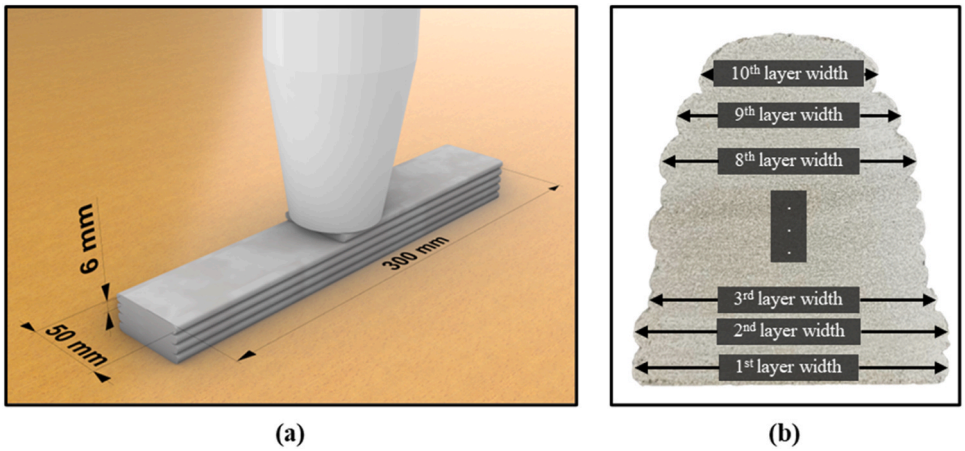
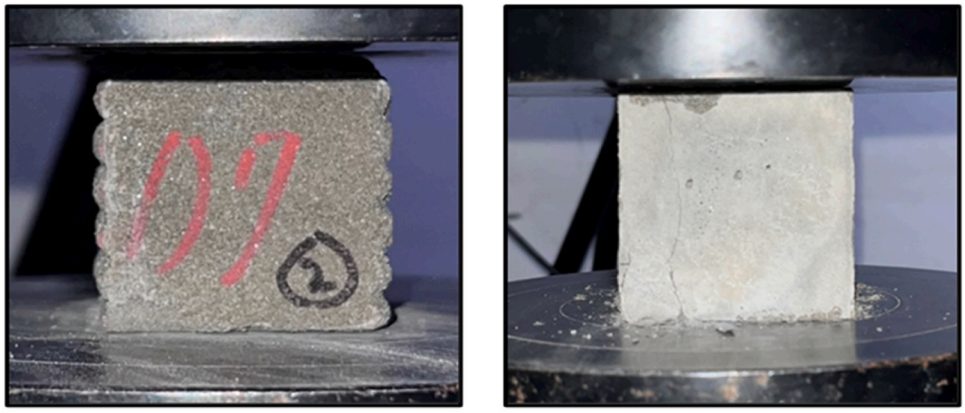
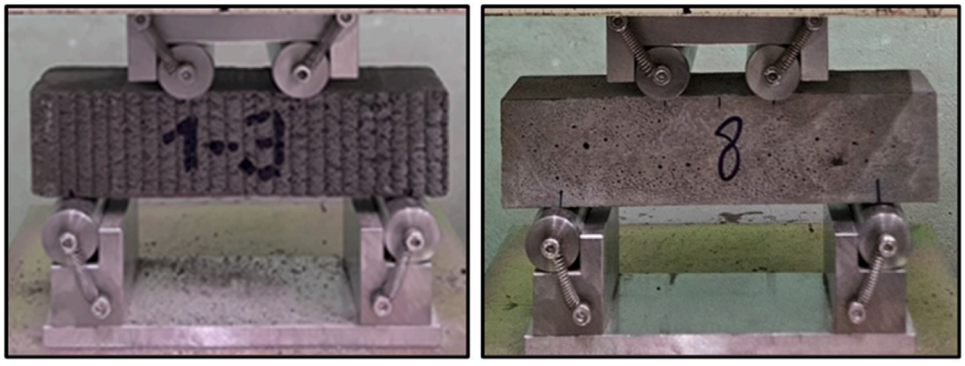


Fig. 4. Simplistic evaluation method to evaluate buildability (a) schematic illustration of the buildability test and (b) exemple of layer width measurement.



(a) (b)

Fig. 5. Compressive strength specimens for 3DPM (a) printed cube specimen, and (b) cast cube specimen.



(a) (b)

Fig. 6. Flexural strength specimens for 3DPM (a) printed beam specimen, and (b) cast beam specimen.

Table 3
28-d mean compressive test results of each specimen type.

Specimens	Mean compressive strength [MPa]	CoV[%]
Printed cube specimen	29.63	24.05
Cast cube specimen	49.88	11.29

Note: *CoV represents covariance

Table 4
28-d flexural test results of each specimen type.

Specimens	Mean flexural strength [MPa]	CoV[%]
Printed beam specimen	3.80	15.00
Cast beam specimen	7.40	10.21

3. Experimental program

3.1. Beam geometries and dimensions

In this study, two 3DPF beams and two cast-in-place (CIP) beams were tested to investigate the flexural behavior of 3DPF. Fig. 7 presents the geometries and dimensions of the beams. Each 3DPF beam consisted of three 900 mm-long 3DPF segments with two

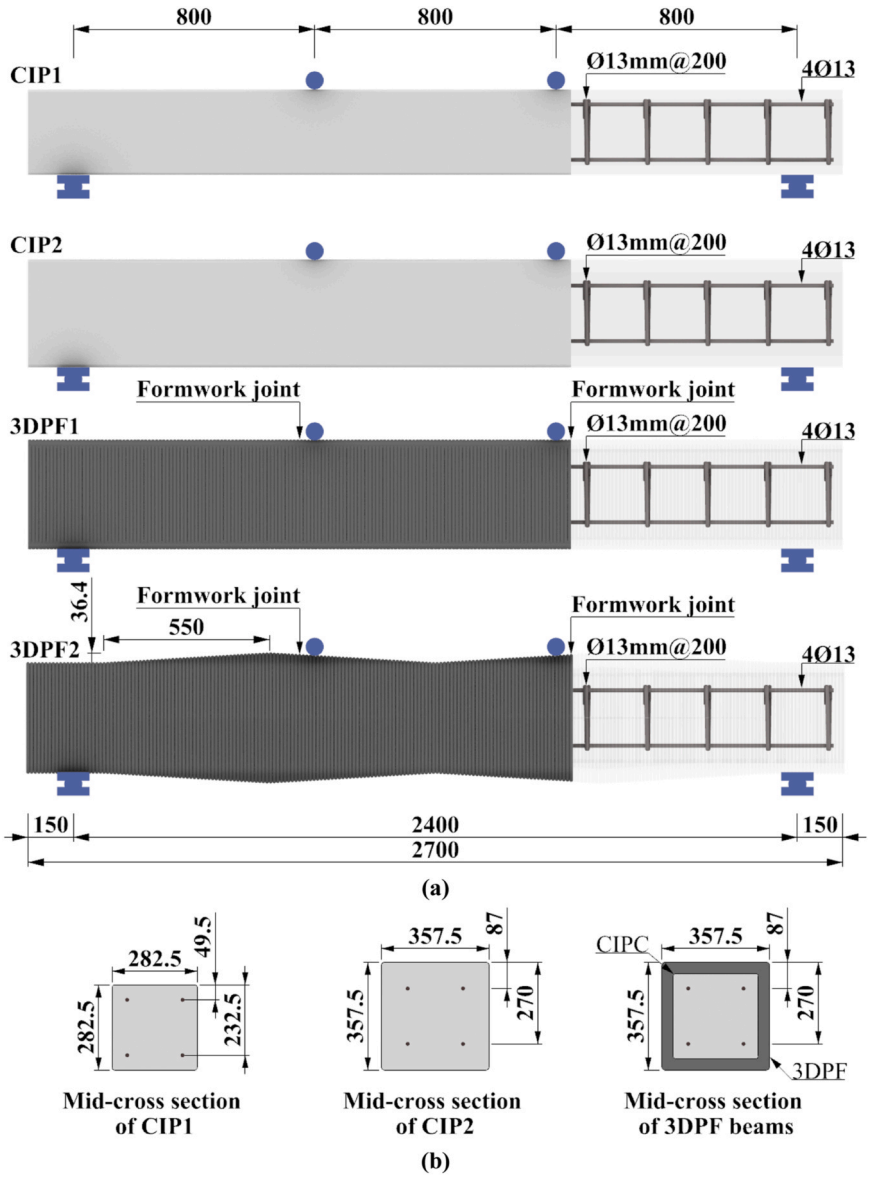


Fig. 7. (a) Overall beam geometries and dimensions, (b) Mid-span cross-sectional dimensions of each beam (all dimensions in mm).

formwork joints. The mid-cross section dimensions of 3DPF1 were 357.5 mm × 357.5 mm, with a 37.5 mm thickness of 3DPF. The second beam, 3DPF2, was designed to evaluate the manufacturability and challenges of 3DCP using an octagonal shape; its dimensions at the supported ends and mid cross-section were the same as those of 3DPF1 (357.5 mm × 357.5 mm).

The mid-cross section of CIP1, the first control beam, was 282.5 mm × 282.5 mm, matching the core concrete dimensions of 3DPF1 to assess the structural effectiveness of the 3DPF cross-section. The cross-section of CIP2 was designed for comparison with the 3DPF beams; its cross-sectional dimensions were the same as those of the 3DPF beams. The cross-section was designed with identical

Table 5
List of specimens.

Specimen ID	Mid-cross section dimensions [mm]			Longitudinal rebars	Stirrup
	Width	Height	3DPF thickness		
CIP1	282.5	282.5	–	4D13	D13@200
CIP2	357.5	357.5	–	4D13	D13@200
3DPF1	357.5	357.5	37.5	4D13	D13@200
3DPF2	357.5	357.5	37.5	4D13	D13@200

dimensions to evaluate the effects of 3DPF on the flexural behavior of RC beams in comparison with CIPC, and to examine the applicability of the existing design code. All beams were reinforced with 13 mm diameter SD500 longitudinal rebars and 13 mm diameter SD400 stirrups with a spacing of 200 mm, respectively. The stirrups were closed with a 135° hook (Table 5). The reinforcement details and spacing were designed according to Eurocode 2 [29]. The SD500 and SD400 rebars are classified according to the Korean standard KS D 3504, which specified characteristic yield strengths of 500 MPa and 400 MPa, respectively [50].

The mean yield stress and strain values are listed in Table 6. The nominal cross sectional area of the rebar was 126.7 mm^2 for both longitudinal rebars and stirrups, and they had the same elastic modulus, $E_s = 200{,}000$ MPa.

3.2. Fabrication process of specimens

Fig. 8 illustrates the fabrication processes for both 3DPF and CIP beams. Materials were mixed for the construction of 3DPF, as described in Section 2.1. After mixing, 3D concrete printing was performed using a self-made three-axis gantry with a maximum printing size of 1000 mm × 1000 mm × 1000 mm and a circular screw nozzle with a diameter of 22.5 mm. The printing parameters included a nozzle speed of 1800 mm/min, nozzle stand-off distance of 6 mm, and flow rate of 2.1 l/min (Table 7). These printing parameters were selected based on the lab-scale preliminary tests described in Section 2.2, with the aim of ensuring the quality of the 3DPF segments. The 3DPF segments were printed to a length of 916 mm, taking into account material deformation and milling joint surfaces. The fabrication process of 3DPF segments was conducted under the same environmental conditions as the lab-scale preliminary tests.

After printing, the upper surfaces of the 3DPF segments were manually milled for assembly. The segments were then wet-cured for 7 days. After curing, the segments were transported to a precast factory and assembled with epoxy after 24 days. The flexural strength of the epoxy was 15 MPa. After an additional 17 days, rebars were placed inside the formwork, and CIPC was poured. Following casting, the beams were steam-cured for 10 days under an average temperature of 65℃. The experiment was conducted 23 d later. For the comparison group, CIP beams were fabricated using temporary formworks and rebars. The CIPC was poured simultaneously with the 3DPF specimens and steam-cured for the same duration.

3.3. Test setup and process

Fig. 9 shows the four-point bending test setup for the beams, which were supported and subjected to a four-point load. The beams were loaded at mid-span and subjected to two concentrated forces applied through a distributive girder with a distance of 800 mm. The beams were supported by hinges with a span length of 2400 mm. Displacement-controlled loading was applied to all beams. Before visible cracks were detected, the loading speed was 0.5 mm/min, which was increased to 2 mm/min once cracking occurred, allowing the load–displacement responses to be recorded. The load was applied until the concrete crushed. Due to uneven side surfaces of the 3DPF beams, it took some time after the start of the experiment for the supports and loading plates to be fully contacted with the specimen and exhibit stable stiffness.

At mid-span, six strain gauges were distributed along the height of the beams, spaced 64 mm apart, to measure concrete strain. In the case of 3DPF2, the strain gauge location was determined to allow placement as close as possible to the center, due to the inward-angled shape at the midsection. The height of the concrete strain gauges was kept consistent across all specimens. Two steel strain gauges were attached at mid-span on the compression and tensile rebars section to measure the strain in the steel rebars. Additionally, vertical mid-span displacement was measured using a linear variable differential transducer (LVDT) for all beams.

4. Experimental results

4.1. Crack pattern and failure mode

Fig. 10 shows a comparison of the side crack patterns between CIP beams and 3DPF beams. From the figure, it is evident that the cracks in the 3DPF beams propagated along the interfaces between printed layers, which is different from the crack patterns observed in the CIP beams. At the failure stage, the crushing of the top concrete was observed in all beams. Additionally, in 3DPF1, approximately 130 mm of the bottom piece, located outside the pure bending section, was delaminated. Fig. 11 illustrates that the 3DPF and CIPC were well bonded, with no separation from the main body. In 3DPF2, a large opening occurred along the central layer at the ultimate load. Although 3DPF2 had the same mid-cross section as 3DPF1, its overall geometry was designed to widen symmetrically away from the center (Fig. 7), resulting in the mid-cross section being the narrowest along the pure bending region. Accordingly, the flexural stiffness in the mid-cross section was the lowest before the cracking, as it had the smallest moment of inertia. While the initial cracking in 3DPF1 occurred at the segment joint, that of 3DPF2 was observed at the center. As a result, the variable cross-section in the

Table 6
Mechanical properties of rebars.

Steel type	Diameter[mm]	Mean yield stressf_y [MPa]	Mean yield strainε_y [με]
SD500	13	584.69	2898.33
SD400	13	449.57	2507.67

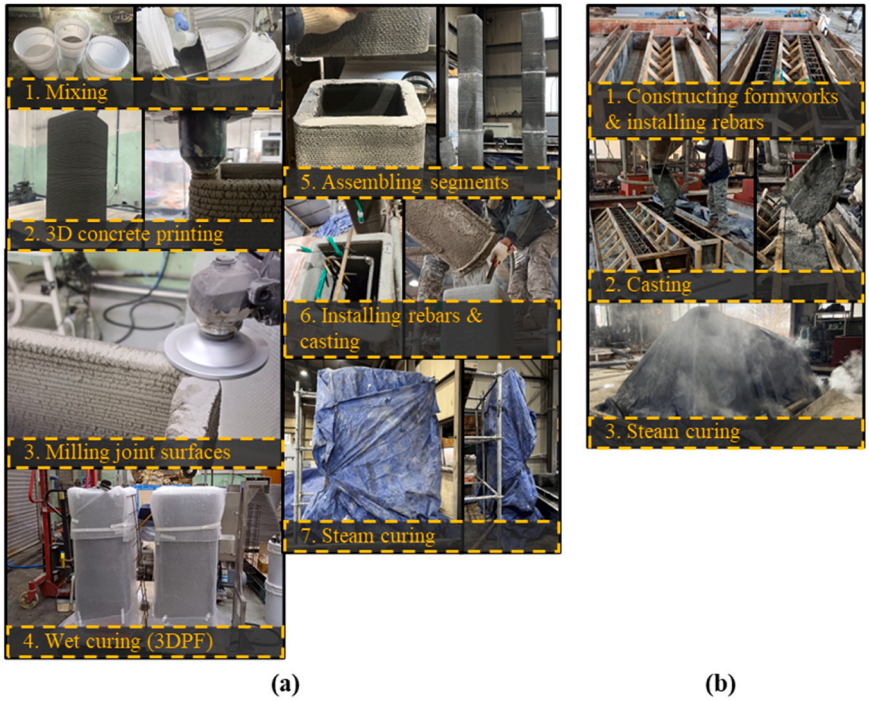


Fig. 8. Fabrication process of (a) 3DPF and (b) CIP beams.

Table 7
Printing parameters used for the fabrication of the 3DPF segments.

Nozzle diameter [mm]	Nozzle speed [mm/min]	Nozzle stand-off distance[mm]	Flow rate[l/min]
22.5	1800	6	2.1

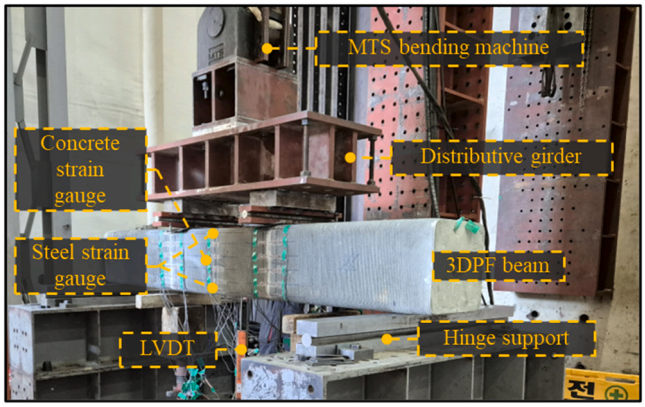


Fig. 9. Test setup for the four-point bending tests.

pure bending section of 3DPF2 led to the progression from the vertical cracking to the large opening failure. This failure progression is similar to that observed in the notched beam test, where the fracture plane is intentionally reduced. These observations demonstrate that even when the mid-cross section is identical, variations in global geometry can significantly affect the failure mode of 3DPF beams.

To investigate the bending failure process of the 3DPF beams, the 3DPF1 was typically selected for a detailed analysis. The crack propagation and failure pattern of 3DPF1 under the four-point bending test are shown in Fig. 12. The first crack appeared in the epoxy used for the formwork joints. Next, a flexural crack developed at the mid-span of the beam when the load reached 36.85 kN. Upon reaching a load of 90.43 kN, the tensile rebar yielded. At a load of 110 kN, the crack that had been propagating vertically along the

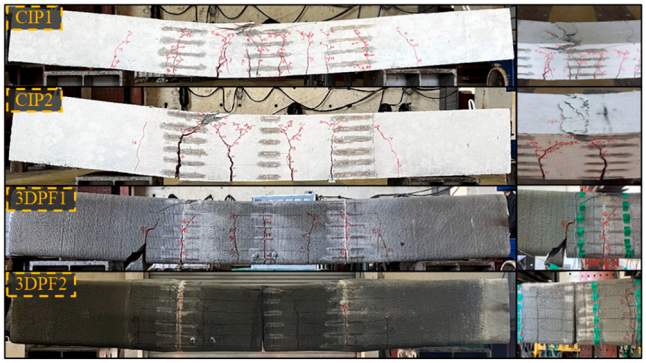


Fig. 10. Failure crack patterns of beams.

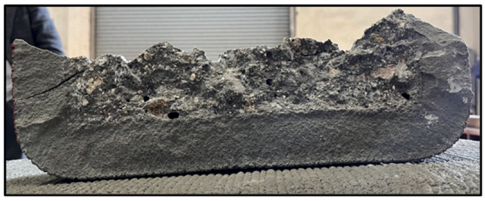


Fig. 11. Delaminated piece from the bottom of 3DPF1.

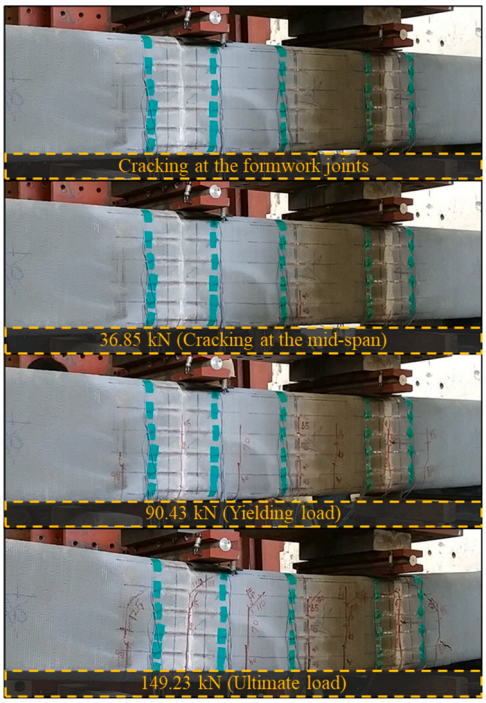


Fig. 12. Flexural failure process of 3DPF1.

layer began to extend upward at a 45° angle. Finally, the compression rebars yielded, the top concrete of 3DPF1 was crushed, and part of the tension side delaminated, leading to failure at a load of 149.23 kN.

4.2. Load–displacement response

The load–displacement relationships at mid-span is shown in Fig. 13. Deflection was measured using an LVDT located at the bottom of the mid-span. All the load–displacement curves of the beams were linear before cracking. After cracking, the curves became nonlinear as the load increased, and the slope gradually decreased. The loading stages were determined using the load–displacement relationships and the load–strain relationships of the tensile rebars at mid-span, as shown in Fig. 14. The performance of the 3DPF group is comparable to that of CIP2, which shares the same cross-sectional dimensions. However, it is evident that the deformation capacity of 3DPF1 and 3DPF2 is lower than that of CIP1 and CIP2.

Fig. 15 presents the enlarged load–displacement relationships for each beam specimen, along with their corresponding secant stiffness. The secant stiffness was evaluated as the slope of each curve at the cracking load. Due to the uneven surface of the 3DPF beams, sufficient loading was required to achieve full contact with the supports and loading plates, resulting in a nonlinear shape in the initial portion of the curve compared to that of the CIP beams. According to the secant stiffness evaluation, 3DPF1 exhibited higher stiffness than CIP2, while 3DPF2 showed lower stiffness than CIP2. Despite the inherent anisotropic characteristic of 3DPF induced by the fabrication method, it did not significantly influence the secant stiffness in flexural behavior.

Table 8 summarizes the flexural test results, including cracking load, yielding load, ultimate load, and deflection at each load. 3DPF offers clear advantages in flexural behavior as permanent formwork. Compared to CIP1, the 3DPF group showed increases in cracking, yielding, and ultimate loads. However, deflection at cracking, yielding, and ultimate loads decreased. When 3DPF was considered not merely as permanent formwork but as a structural member and compared to CIP2, both 3DPF1 and 3DPF2 exhibited flexural capacities nearly identical to that of CIP2 but demonstrated lower cracking loads. This behavior is attributed to the anisotropic properties of the 3DPF.

Moreover, the ductility was evaluated from the perspective of structural resilience. The displacement ductility index, which is the ratio of the yielding load to the ultimate load displacement, was compared for each beam, as presented in Table 8. The 3DPF group exhibited higher ductility compared to CIP1 but lower ductility compared to CIP2. This result indicates that, despite the beam specimens having identical cross-sectional dimensions and geometry, differences in the top material caused variations in ultimate strain, leading to differences in ductility [51]. Additionally, the large opening failure mode observed in 3DPF2 resembled a brittle failure, resulting in reduced deformation capacity compared to 3DPF1. Consequently, a noticeable difference in ductility was observed between 3DPF1 and 3DPF2.

4.3. Strain distributions of beams

The lines depicted in Fig. 16 represent the results obtained from strain gauges placed sequentially at predetermined heights along the side of the mid-span of 3DPF1 and 3DPF2. The gauges were used to observe whether the 3DPF behaved integrally within the entire tests without debonding. The boundary between the 3DPF and CIPC marked by yellow lines in Fig. 16. Owing to crack propagation, data from the gauges located at the lower section were lost. However, the remaining gauge data and visual observations during the experiment confirmed that as the load increased, the neutral axis shifted upward. This indicates that the strain distribution in the 3DPF beams adhered to the plane section assumption from the beginning of loading until reaching the ultimate load. The position of the neutral axis was determined using strain distribution graphs and measurements taken from the beams post-four-point bending tests. At the ultimate load, the neutral axis was located 22 mm from the top in 3DPF1 and 23 mm from the top in 3DPF2. Compared to the CIP2 beam, whose neutral axis was located 27.7 mm from the top at the ultimate load, the neutral axes of the 3DPF beams were located

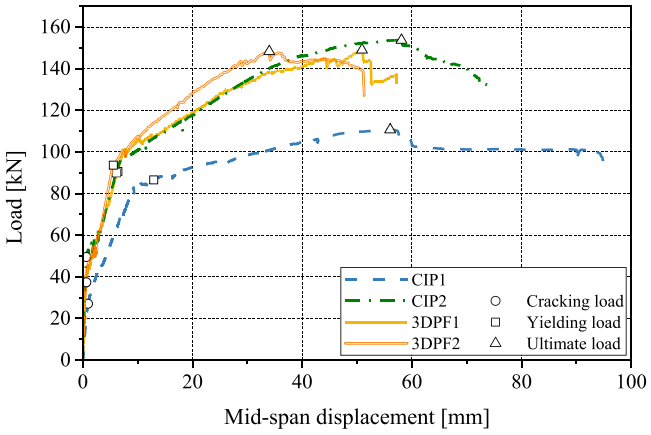


Fig. 13. Load–displacement relationships at the mid-span.

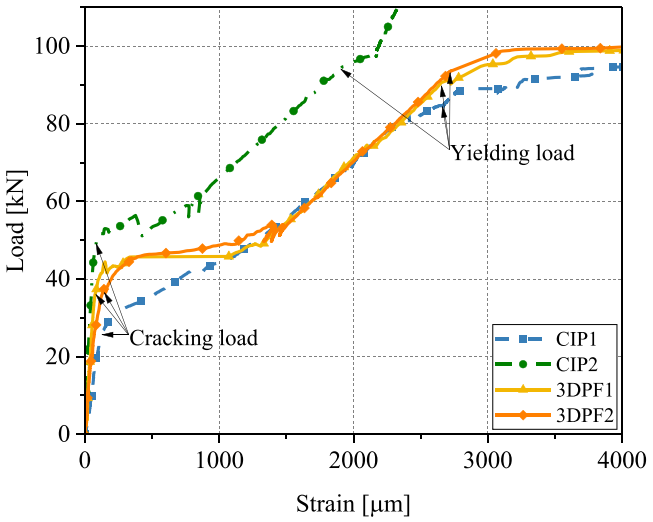


Fig. 14. Load–strain relationships of the tensile rebar at the mid-span.

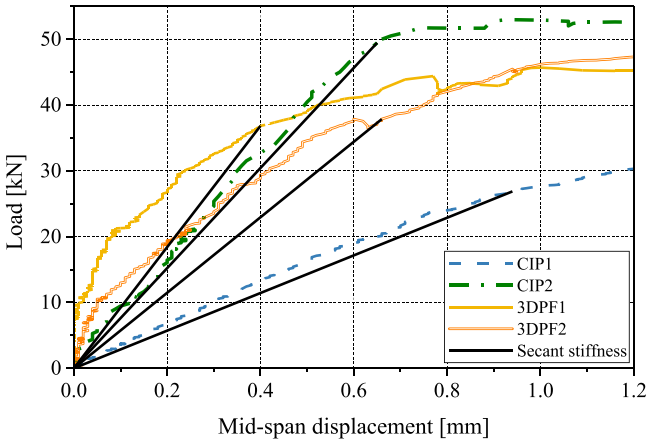


Fig. 15. Secant stiffness at the cracking load for each beam specimen.

Table 8
Flexural test results of beams.

Specimen ID	Cracking load [kN]	Yielding		Ultimate		Secant stiffness ratio	Displacement ductility index ratio
		Load[kN]	Displ.[mm]	Load[kN]	Displ.[mm]		
CIP1	26.89	86.02	12.57	110.65	56.22	0.38	0.5
CIP2	49.48	93.22	6.46	153.67	58.11	1	1
3DPF1	36.85	90.43	6.39	149.23	50.99	1.21	0.89
3DPF2	37.88	93.57	5.54	148.42	33.89	0.75	0.68

higher.

5. Analytical calculation of the nominal flexural strength

In this study, the nominal flexural strength of the 3DPF beam cross sections was calculated using the strain compatibility method to clarify the key elements required for extending this study toward nonlinear analysis of 3DPF structures and to bridge the gap between their behavior and existing design codes. All 3DPF beams conformed to the plane section assumption before reaching the ultimate load. First, incorporating the fabrication characteristics of 3DCP into the member's sectional analysis is necessary. During printing, material deformation causes the upper layers to become narrower while both sides expand outward. Consequently, as shown in Fig. 17, expanded sections due to layer deposition are formed, which do not contribute to the flexural behavior of the formwork. To exclude

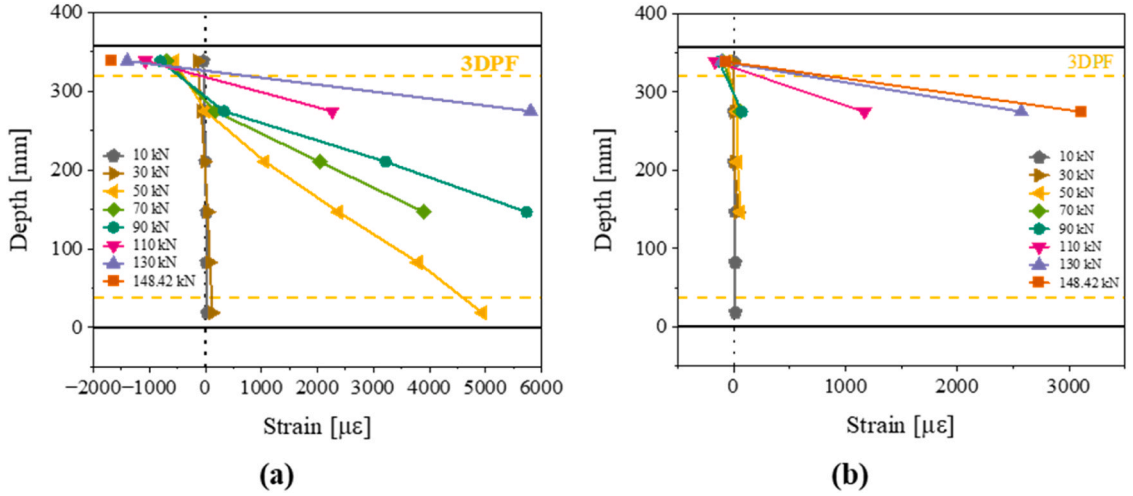


Fig. 16. Strain distribution at the mid-span of beams (a) 3DPF1 and (b) 3DPF2.

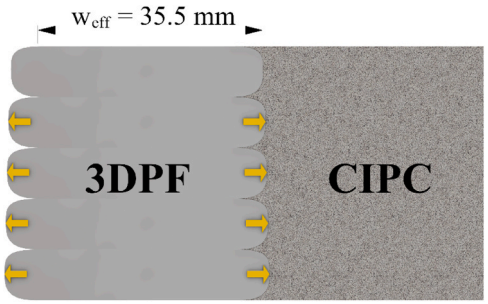


Fig. 17. Definition of the effective width for 3DPF beams.

these noncontributing expanded regions from the force calculations, the topmost and thinnest width of the 3DPF section was measured after the joint surfaces were milled, and the outwardly expanded parts were removed, thereby defining the layer effective width (w_{eff}). In this study, the layer width was 37.5 mm, and the effective layer width was 35.5 mm. The ratio of the effective layer width to the layer width was 95 %.

As no specific design guidelines exist for members fabricated with 3DCP, this study used the parabola–rectangular (p–r) stress–-strain relationship for concrete in compression (as defined in Eurocode 2 and shown in Fig. 18**(a)**) and an idealized stress–strain curve for reinforcing steel without tension-hardening effects after yielding (Fig. 18**(b)**) [29] to evaluate the applicability of Eurocode 2. Fig. 17(a) can be described by Eq. (4) [52].

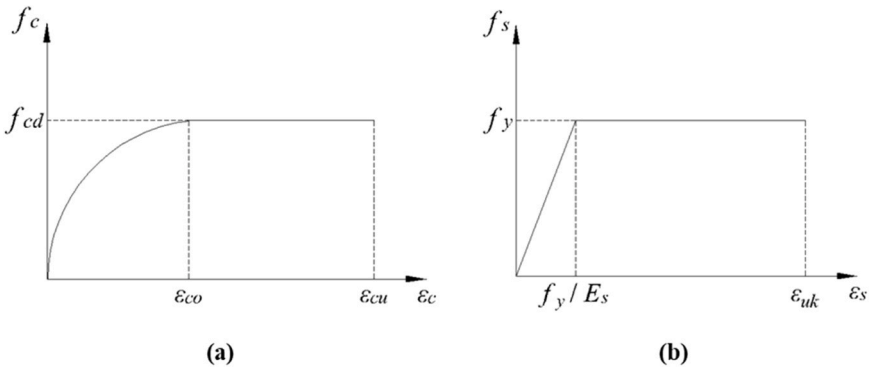


Fig. 18. Stress–strain models of (a) parabola–rectangular (p–r) curve for 3DPM and CIPC, and (b) idealized curve for the rebar in Eurocode 2.

$$f_c = \begin{cases} f_{cd}\left[1 - \left(\frac{\varepsilon_c}{\varepsilon_{c0}}\right)^n\right] for, \quad (0 \le \varepsilon_c \le \varepsilon_{c0}) \\ f_{cd} for, \quad (\varepsilon_{c0} \le \varepsilon_c \le \varepsilon_{cu}) \end{cases} \tag{4}$$

Here, ε_{cu} is the ultimate strain, taken as 0.0035, and ε_{c0}, the strain at the peak stress, is 0.002 for normal-strength concrete with a characteristic compressive strength (f_{ck}) of 50 MPa or less. The exponent n, which defines the shape of the ascending branch of the curve, is 2.0. The design compressive strength f_{cd} is given by Eq. (5). However, in this study, the mean compressive strengths of 3DPM and CIPC were used instead.

$$f_{cd} = 0.85 f_{ck} \tag{5}$$

$for,\ 0 \le \varepsilon_c \le \varepsilon_{c0}$

$$\alpha = \frac{\varepsilon_c(6 - \varepsilon_c)}{12} \tag{6}$$

$$\beta = \frac{8 - \varepsilon_c}{4(6 - \varepsilon_c)} \tag{7}$$

$for,\ \varepsilon_{c0} \le \varepsilon_c \le \varepsilon_{cu}$

$$\alpha = \frac{3\varepsilon_c - 2}{3\varepsilon_c} \tag{8}$$

$$\beta = \frac{8 - \varepsilon_c}{4(6 - \varepsilon_c)} \tag{9}$$

where α is the dimensionless coefficient representing the average stress over the neutral axis depth and β is the dimensionless coefficient representing the location of the compressive force centroid. These two coefficients are obtained by integrating Eq. (4) and can be expressed as in Eqs. (6)–(9) [52]. These coefficients were applied to compute the internal forces with subscripts for each part of the cross-section.

Fig. 19 shows the cross-section and the combined forces of 3DPF beams corresponding to different locations of the neutral axis (c). Depending on the position of the neutral axis, the location of compressive force centroids, and the directions of forces of 3DPF, CIPC,

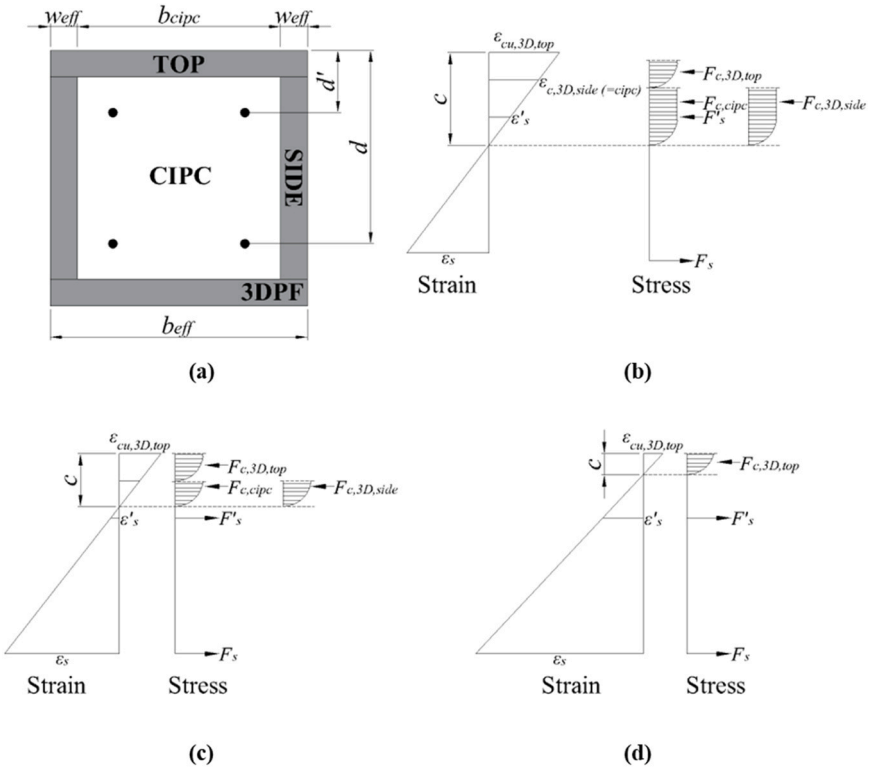


Fig. 19. Stress and strain distribution at the ultimate stages: (a) cross-section of 3DPF beams with effective width; cases of (b) $d' \le c$, (c) $w_{eff} < c < d'$, and (d) $c \le w_{eff}$.

and the compression rebars varied. In this study, the ultimate compressive strain at the top of 3DPF was represented as $\varepsilon_{cu,\ 3D,top}$ and assumed to be 0.0035 following Eurocode 2. Using $\varepsilon_{cu,\ 3D,top}$, the upper strain of the 3DPF side parts ($\varepsilon_{cu,\ 3D,side}$), CIPC ($\varepsilon_{c,cipc}$), the tensile rebars ($\varepsilon_s$), and the compression rebars ($\varepsilon_s^{'}$) were determined, and the corresponding forces were expressed as presented in Table 9. The expressions $f_{c,3D}$ and $f_{c,cipc}$ represented the compressive stresses of the 3DPM and CIPC, respectively, both derived from the p–r curve. The term b_{eff} refered to the effective width of the 3DPF, and b_{cipc} refered to the width of CIPC. The parameters d and $d^{'}$ denoted the effective depths to the tensile and compression rebars, respectively, and A_s and $A_s^{'}$ indicated the nominal areas of the tensile and compression rebars, respectively. The tensile strengths of the 3DPF and CIPC were not considered in this analysis.

When the sum of forces equals zero, the nominal flexural moment can be determined using Eqs. (10)–(12). Finally, the nominal flexural strength can be calculated using Eq. (13).

$$M_n = F_{c,3D,top}\left(d-\beta_{3D,top}w_{eff}\right)+F_{c,3D,side}\left(d-w_{eff}-\beta_{3D,side}\left(c-w_{eff}\right)\right)+F_s^{'}(d-d^{'})+F_{c,cipc}\left(d-w_{eff}-\beta_{cipc}\left(c-w_{eff}\right)\right) for, \quad (d^{'}\le c) \tag{10}$$

$$M_n = F_{c,3D,top}\left(d-\beta_{3D,top}w_{eff}\right)+F_{c,3D,side}\left(d-w_{eff}-\beta_{3D,side}\left(c-w_{eff}\right)\right)-F_s^{'}(d-d^{'})+F_{c,cipc}\left(d-w_{eff}-\beta_{cipc}\left(c-w_{eff}\right)\right) for, \quad \left(w_{eff}<c<d^{'}\right) \tag{11}$$

$$M_n = F_{c,3D,top}\left(d-\beta_{3D,top}c\right)-F_s^{'}(d-d^{'}) for, \quad (c\le w_{eff}) \tag{12}$$

$$P_n = 2.5M_n \tag{13}$$

Table 10 presents the results of nominal flexural strength calculations. Compared with the experimental results, the calculations achieved an average accuracy of approximately 92.5 %. Additionally, consistent with the experimental results, the calculated neutral axis was located 35 mm within the 3DPF layer, and the compression reinforcement yielded. The agreement between experimental and analytical resultscan be explained by the fact that, although Eurocode 2 does not fully reflect the characteristics of the printed material, this study compensated for such limitations by incorporating the experimentally obtained equivalent strength of the printed material, the concept of effective layer width, and the actual cross-sectional geometry into the section analysis. In other words, while a complete material modeling approach was not applied, the structural characteristics of 3DPF were partially considered in the analysis, contributing to the high consistency between experimental and calculated results.

The difference between the calculated and measured flexural nominal strengths is attributed to the high uncertainty stemming from the quality of the printed material and the concentration of cracks along the layer interfaces. Furthermore, current design codes do not account for the unique characteristics of the printing material. Specifically, the stress–strain model and the ultimate strain proposed in Eurocode 2 were developed based on accumulated data from conventional concrete that contains coarse aggregates and is cast monolithically. In contrast, the printed material used in this study contains no coarse aggregates and was fabricated using a layer-by-layer deposition method. As a result, it is expected to exhibit a different relationship between elastic modulus and compressive strength compared to conventional concrete, as well as anisotropic behavior along the layer directions. This anisotropy was confirmed in Section 2.3. by comparing the compressive strengths of printed and cast cube specimens. Due to these differences in material characteristics, the stress–strain behavior and the ultimate strain of the printed material is likely to differ from that of conventional concrete, which may serve as potential reasons of errors when applying the strain compatibility method. Therefore, if such characteristics are considered, the accuracy of the analysis using the strain compatibility method could be further improved.

6. Conclusions

This study investigated and analyzed the effects of 3DPF on the flexural behavior of RC beams. Four-point bending tests were

Table 9
Strain and force calculations following the locations of the neutral axis.

Case	Strain	Force
$d^{'}\le c$	$\varepsilon_{c,3D,side}=\varepsilon_{c,cipc}=\varepsilon_{c,3D,top}\frac{(c-w_{eff})}{c}$ $\varepsilon_s=\varepsilon_{cu,3D,top}\frac{(d-c)}{c}$ $\varepsilon_s^{'}=\varepsilon_{cu,3D,top}\frac{(c-d^{'})}{c}$	$F_c=\begin{cases}F_{c,3D,top}=\alpha_{3D,top}f_{c,3D}b_{eff}w_{eff}\\ F_{c,3D,side}=\alpha_{3D,side}f_{c,3D}(2w_{eff})(c-w_{eff})\\ F_{c,cipc}=\alpha_{cipc}f_{c,cipc}b_{cipc}(c-w_{eff})\end{cases}$ $F_s=\begin{cases}A_s\varepsilon_sE_s(\varepsilon_s<\varepsilon_y)\\ A_sf_y(\varepsilon_y\le\varepsilon_s)\end{cases}$ $F_s^{'}=\begin{cases}A_s^{'}\varepsilon_sE_s(\varepsilon_s<\varepsilon_y)\\ A_s^{'}f_y(\varepsilon_y\le\varepsilon_s)\end{cases}$
$w_{eff}<c<d^{'}$	$\varepsilon_{c,3D,side}=\varepsilon_{c,cipc}=\varepsilon_{c,3D,top}\frac{(c-w_{eff})}{c}\varepsilon_s=\varepsilon_{cu,3D,top}\frac{(d-c)}{c}\varepsilon_s^{'}=\varepsilon_{cu,3D,top}\frac{(d^{'}-c)}{c}$	F_c and F_s are the same as in $d^{'}\le c$, except $F_s^{'}$ is tensile.
$c\le w_{eff}$	$\varepsilon_{c,3D,side}=\varepsilon_{c,cipc}=\varepsilon_{c,3D,top}\frac{(w_{eff}-c)}{c}\varepsilon_s=\varepsilon_{cu,3D,top}\frac{(d-c)}{c}\varepsilon_s^{'}=\varepsilon_{cu,3D,top}\frac{(d^{'}-c)}{c}$	$F_c=F_{c,3D,top}=\alpha_{3D,top}f_{c,3D}b_{eff}c$ F_s and $F_s^{'}$ are the same as in $w_{eff}<c<d^{'}$.

Table 10
Calculated nominal flexural strength of 3DPF beams.

Specimen ID	Experiment [kN]	Calculated nominal flexural strength[kN]	Experiment/Calculation
3DPF1	149.23	160	0.93
3DPF2	148.42		0.92

conducted on 3DPF beams, and the failure modes, load–displacement responses, and strain distributions of the beams were evaluated. Analytical calculations were compared with experimental results, leading to the following conclusions:

1. The equivalent strengths between cast and printed material beams were estimated through mechanical property tests on 3DPM, providing a basis for analyzing 3DPF beams. These equivalent strengths are also critical for member quality control and could be further developed into empirical formulas if additional beams with varying printing orientations are included.
2. A fabrication process for 3DPF beams, including milling the joint surfaces of 3DPF segments, was proposed. However, owing to the lack of joint details, the first cracks formed at the epoxy joints rather than at the mid-span.
3. The ultimate flexural strengths of 3DPF beams were significantly higher than that of CIP1 and were nearly identical to that of CIP2. Therefore, it can be concluded that incorporating a 3DPF cross-section in the strength design of a flexural member is a structurally effective approach.
4. The inherent properties of 3DPF, particularly its anisotropic behavior and interlayer characteristics, notably influenced the flexural behavior of the 3DPF beams. Although the 3DPF itself had no significant impact on the secant stiffness prior to cracking, their layer interfaces contributed to the formation of vertical cracks along these interfaces and caused lower cracking loads compared to those of the CIP beams. Furthermore, the displacement ductility values of the 3DPF beams were lower than those of the CIP beams, indicating that the ultimate strain of the printed material is lower than that of CIPC. In particular, the superposition of vertical cracking propagation and the variable cross-section of 3DPF2 triggered the large opening failure mode, which further diminished its displacement ductility. These findings indicate that enhancing reinforcement at the layer interfaces or adopting a more conservative design approach compared to the CIPC structures is necessary to mitigate such limitations.
5. The strain compatibility method, incorporating section analysis for 3DPF beams, the experimentally obtained equivalent strength of the printed material, and the concept of effective layer width, was proposed. The values calculated using this method aligned well with the experimental results regarding nominal flexural strength and neutral axis depth, thereby providing a preliminary basis for developing nonlinear analysis methods and for establishing design codes and specifications applicable to 3DPF structures beyond just 3DPF beams.

The fabrication methods of this study can be further extended to other structural members such as columns and walls. For the more accurate fabrication and analysis of 3DPF members, future studies will focus on developing a geometry control process with the surface milling process to replace the match casting technology and defining formwork joint reinforcement details to ensure the accurate and robust assembly of 3DPF segments. The development of standardized stress–strain models and strength testing methods should be prioritized, as they serve as fundamental links between design codes and specifications, ultimately contributing to quality control. Once a clear guideline is established, these stress–strain curves can be incorporated into existing design codes—such as in the strain compatibility method proposed in this study. Furthermore, data of printed materials can be systematically and reliably accumulated based on standardized strength testing methods.

CRediT authorship contribution statement

Tae-Kyung Kim: Writing – review & editing, Writing – original draft, Visualization, Methodology, Investigation, Formal analysis, Data curation, Conceptualization. **Dong Wonjun:** Writing – original draft, Methodology, Investigation. **Bunleang Mak:** Writing – original draft, Methodology, Investigation. **Sangwoo Oh:** Writing – original draft, Methodology, Conceptualization. **Jinsuk Lee:** Investigation, Data curation. **Seongcheol Choi:** Writing – review & editing, Conceptualization. **Shim Changsu:** Writing – review & editing, Supervision, Resources, Project administration, Funding acquisition, Formal analysis.

Declaration of Competing Interest

This manuscript has not been published or presented elsewhere in part or entirely and is not under consideration by another journal. We have read and understood your journal's policies, and we believe that neither the manuscript nor the study violates any of these. There are no conflicts of interest to declare.

Acknowledgements

This research was conducted with the support of the "National R&D Project for Smart Construction Technology (RS-2020-KA156007)" funded by the Korea Agency for Infrastructure Technology Advancement under the Ministry of Land, Infrastructure and Transport, and managed by the Korea Expressway Corporation. Additionally, this research was supported by the Chung-Ang University

Graduate Research Scholarship in 2024.

Data availability

Data will be made available on request.

References

[1] B.B. Akomah, L.K. Ahinaquah, Z. Mustapha, Skilled Labour Shortage in the Building Construction Industry Within the Central Region, in: Baltic Journal of Real Estate Economics and Construction Management, 8, Riga Technical University, 2020, pp. 83–92, https://doi.org/10.2478/bjreecm-2020-0006.
[2] S.L. Zulu, A.M. Saad, T. Omotayo, The mediators of the relationship between digitalisation and construction productivity: a systematic literature review, Buildings 13 (4) (2023) 839.
[3] A.E. Oke, J. Aliu, P.O. Fadamiro, P.O. Akanni, S.S. Stephen, Attaining digital transformation in construction: an appraisal of the awareness and usage of automation techniques, J. Build. Eng. 67 (2023) 105968.
[4] S.C. Paul, G.P. Van Zijl, M.J. Tan, I. Gibson, A review of 3D concrete printing systems and materials properties: Current status and future research prospects, Rapid Prototyp. J. 24 (4) (2018) 784–798.
[5] J. Xiao, G. Ji, Y. Zhang, G. Ma, V. Mechtcherine, J. Pan, S. Du, Large-scale 3D printing concrete technology: Current status and future opportunities, Cem. Concr. Compos 122 (2021) 104115.
[6] A. du Plessis, A.J. Babafemi, S.C. Paul, B. Panda, J.P. Tran, C. Broeckhoven, Biomimicry for 3D concrete printing: A review and perspective, Addit. Manuf. 38 (2021) 101823.
[7] J. Zhang, J. Wang, S. Dong, X. Yu, B. Han, A review of the current progress and application of 3D printed concrete, Compos. Part A Appl. Sci. Manuf. 125 (2019) 105533.
[8] F. Bos, R. Wolfs, Z. Ahmed, T. Salet, Additive manufacturing of concrete in construction: Potentials and challenges of 3D concrete printing, Virtual Phys. Prototyp. 11 (3) (2016) 209–225.
[9] P. Wu, J. Wang, X. Wang, A critical review of the use of 3-D printing in the construction industry, Autom. Constr. 68 (2016) 21–31.
[10] A. Siddika, M.A.A. Mamun, W. Ferdous, A.K. Saha, R. Alyousef, 3D-printed concrete: Applications, performance, and challenges, J. Sustain. Cem. -Based Mater. 9 (3) (2020) 127–164.
[11] A.H. Alami, A.G. Olabi, M. Ayoub, H. Aljaghoub, S. Alasad, M.A. Abdelkareem, 3D concrete printing: recent progress, applications, challenges, and role in achieving sustainable development goals, Buildings 13 (4) (2023) 924.
[12] H. Liu, J. Xiao, T. Ding, Flexural performance of 3D-printed composite beams with ECC and recycled fine aggregate concrete: experimental and numerical analysis, Eng. Struct. 283 (2023) 115865.
[13] J. Cai, Z. Sheng, X. Wang, Y. Fang, J. Pan, Effect of reinforcement configurations on the flexural behaviors of 3D printed fiber reinforced cementitious composite (FRCC) beams, J. Build. Eng. 46 (2022) 103773.
[14] L. Breseghello, H. Hajikarimian, H.B. Jørgensen, R. Naboni, 3DLightBeam+ : Design, simulation, and testing of carbon-efficient reinforced 3D concrete printed beams, Eng. Struct. 292 (2023) 116511.
[15] A. Aramburu, I. Calderon-Uriszar-Aldaca, I. Puente, Wet joint performance of 3D printed concrete beam segments under flexural loading, J. Build. Eng. 73 (2023) 106728.
[16] D. Asprone, F. Auricchio, C. Menna, V. Mercuri, 3D printing of reinforced concrete elements: technology and design approach, Constr. Build. Mater. 165 (2018) 218–231.
[17] M. Qiu, Y. Qian, J.G. Dai, Enhancing the flexural performance of concrete beams with 3D-printed UHP-SHCC permanent formwork via graded fiber volume fraction, Compos. Struct. (2024) 118211.
[18] B. Ter Haar, J. Kruger, G. van Zijl, Off-site 3D printed concrete beam design and fabrication, J. Build. Eng. 89 (2024) 109117.
[19] B. Ter Haar, J. Kruger, G. van Zijl, Off-site construction with 3D concrete printing, Autom. Constr. 152 (2023) 104906.
[20] Y. Asghari, S.E. Mohammadyan-Yasouj, M. Petrů, H. Ghandvar, S.S. R. Koloor, 3D printing and implementation of engineered cementitious composites – a review, Case Stud. Constr. Mat. 21 (2024) e03462, https://doi.org/10.1016/j.cscm.2024.e03462.
[21] L. Pham, P. Tran, J. Sanjayan, Steel fibres reinforced 3D printed concrete: influence of fibre sizes on mechanical performance, Constr. Build. Mater. 250 (2020) 118785, https://doi.org/10.1016/j.conbuildmat.2020.118785.
[22] X. Li, M. Newlands, R. Jones, Performance of a multi-layer aligned steel fibre reinforced concrete beam: A preliminary investigation towards 3D printing, Case Stud. Constr. Mat. 21 (2024) e03615, https://doi.org/10.1016/j.cscm.2024.e03615.
[23] Y. Li, H. Wu, X. Xie, L. Zhang, P.F. Yuan, Y.M. Xie, FloatArch: a cable-supported, unreinforced, and re-assemblable 3D-printed concrete structure designed using multi-material topology optimization, Addit. Manuf. 81 (2024) 104012.
[24] T. Ding, J. Xiao, V. Mechtcherine, Microstructure and mechanical properties of interlayer regions in extrusion-based 3D printed concrete: A critical review, Cem. Concr. Compos 141 (2023) 105154.
[25] H. Tu, Z. Wei, A. Bahrami, N.B. Kahla, A. Ahmad, Y.O. Özkılıç, Recent advancements and future trends in 3D printing concrete using waste materials, Dev. Built Environ. (2023) 100187.
[26] A.U. Rehman, A. Perrot, B.M. Birru, J.H. Kim, Recommendations for quality control in industrial 3D concrete printing construction with mono-component concrete: A critical evaluation of ten test methods and the introduction of the performance index, Dev. Built Environ. 16 (2023) 100232.
[27] V. Mechtcherine, K. van Tittelboom, A. Kazemian, E. Kreiger, B. Nematollahi, V.N. Nerella, M. Santhanam, G. de Schutter, G. Van Zijl, D. Lowke, E. Ivaniuk, M. Taubert, F. Bos, A roadmap for quality control of hardening and hardened printed concrete, Cem. Concr. Res. 157 (2022) 106800.
[28] A. Kumbasaroglu, E. Korkmaz, Effect of longitudinal circular hollows on the flexural strength of reinforced concrete beams, KSCE J. Civ. Eng. 28 (1) (2024) 275–287, https://doi.org/10.1007/s12205-023-0424-2.
[29] European Committee for Standardization, EN 1992–1-1: Eurocode 2: Design of Concrete Structures - Part 1–1: General Rules and Rules for Buildings (2004).
[30] ACI 318 Committee, Building Code Requirements for Structural Concrete, American Concrete Institute, Farmington Hills, MI (2005).
[31] J.S. Kim, J.Y. Lee, Y.H. Kim, D. Kim, J. Kim, J.G. Han, Evaluating the eco-compatibility of mortars with feldspar-based fine aggregate, Case Stud. Constr. Mat. 16 (2022) e00781.
[32] P. Shoaei, H. Gallantree-Smith, V.M. Pacheco, R. Pamies, A.L. Kjøniksen, S. Pilehvar, Comparative analysis of 3D printing of Portland cement mortars with hydroxypropyl methylcellulose and microfibrillated cellulose as viscosity modifying agents, Mater. Des. 244 (2024) 113124.
[33] Iman Mehdipour, Kamal H. Khayat Effect of particle-size distribution and specific surface area of different binder systems on packing density and flow characteristics of cement paste, Cem. Concr. Compos.78 (2017): 120-131..
[34] Y. Tan, M. Dahlenburg, J. Fottner, S. Kessler, Influencing factors of the mixing performance of a near-nozzle continuous mixer for 3D concrete printing: an analysis based on spatial Lacey mixing index (SLMI), Powder Technol. 403 (2022) 117414.
[35] ASTM, C39/C39M: Standard Test Method for Compressive Strength of Cylindrical Concrete Specimens, ASTM International, West Conshohocken, PA, (2018).
[36] ASTM, C1437: Standard test method for flow of hydraulic cement mortar, (2007).
[37] ASTM C403/C403M: Standard Test Method for Time of Setting of Concrete Mixtures by Penetration Resistance, American Society of Testing and Materials West Conshohocken, PA, USA, (2020).
[38] Germann Instruments A/S. ICAR Plus Concrete Rheometer Manual. Emdrupvej 102, DK-2400 Copenhagen, Denmark (2021).

[39] S. Oh, S. Choi, Effects of superabsorbent polymers (SAP) on the rheological behavior of cement mortars: a rheological study on performance requirements for 3D printable cementitious materials, Constr. Build. Mater. 392 (2023) 131856.
[40] S. Oh, G. Hong, S. Choi, Determining the effect of superabsorbent polymers, macrofibers, and resting time on the rheological properties of cement mortar using analysis of variance (ANOVA): a 3D printing perspective, J. Build. Eng. 75 (2023) 106967.
[41] D. Feys, J.E. Wallevik, A. Yahia, K.H. Khayat, O.H. Wallevik, Extension of the Reiner-Riwlin equation to determine modified Bingham parameters measured in coaxial cylinders rheometers, Mater. Struct. 46 (1) (2013) 289–311.
[42] A. Fasihi, N.A. Libre, From pumping to deposition: a comprehensive review of test methods for characterizing concrete printability, Constr. Build. Mater. 414 (2024) 134968.
[43] J.T. Kolawole, D. De-Becker, J. Xu, J. Dobrzanski, S. Cavalaro, S. Austin, N. Roussel, R. Buswell, Selected test methods for assessing fresh and plastic-state 3D concrete printing materials, in: R. Buswell, A. Blanco, S. Cavalaro, P. Kinnell (Eds.), Third RILEM International Conference on Concrete and Digital Fabrication. DC, 37, Springer, Cham, 2022, pp. 460–466.
[44] N. Ducoulombier, R. Mesnil, P. Carneau, L. Demont, H. Bessaies-Bey, J.F. Caron, N. Roussel, The “Slugs-test” for extrusion-based additive manufacturing: Protocol, analysis and practical limits, Cem. Concr. Compos 121 (2021) 104074.
[45] M. Sando, D. Stephan, The development of a fly ash-based geopolymer for extrusion-based 3D printing, along with a printability prediction method, Case Stud. Constr. Mater. 21 (2024) e03407, https://doi.org/10.1016/j.cscm.2024.e03407.
[46] ASTM, C109/C109M: Standard test method for compressive strength of hydraulic cement mortars (using 2-in or [50-mm] cube specimens). Annual Book of ASTM Standards, (2005) vol. 04.01.
[47] ASTM, C348–18: Standard test method for flexural strength of hydraulic cement mortars; ASTM International: West Conshohocken, PA, USA, (2019).
[48] A. Kazemian, B. Khoshnevis, Real-time extrusion quality monitoring techniques for construction 3D printing, Constr. Build. Mater. 303 (2021) 124520.
[49] I. Harbouz, A. Yahia, E. Roziere, A. Loukili, Printing quality control of cement-based materials under flow and rest conditions, Cem. Concr. Compos 138 (2023) 104965.
[50] KS D 3504: Steel bars for concrete reinforcement; Korean Agency for Technology and Standards: Republic of Korea, (2021).
[51] A.J. Kappos, M.K. Chryssanthopoulos, C. Dymiotis, Uncertainty analysis of strength and ductility of confined reinforced concrete members, Eng. Struct. 21 (3) (1999) 195–208.
[52] E. Joshef, Karlsruhe. Concrete Structures Euro-Design Handbook, Ernst & Sohn, 1994, pp. 237–250.